Nano Energy 98 (2022) 107295

Contents lists available at ScienceDirect

Nano Energy

journal homepage: www.elsevier.com/locate/nanoen

Mg/seawater batteries driven self-powered direct seawater electrolysis systems for hydrogen production

Yingshuang Xu [a,1], Honghao Lv [a,1], Huasen Lu [a], Qinghao Quan [a], Wenzhen Li [b], Xuejing Cui [a], Guangbo Liu [a,*], Luhua Jiang [a,*]

[a] Nanomaterial & Electrocatalysis Laboratory, College of Materials Science and Engineering, Qingdao University of Science and Technology, Qingdao 266042, PR China
[b] Department of Chemical & Biological Engineering, Iowa State University, Ames, IA 50011-1098, Unites States

ARTICLE INFO

Keywords:
Mg/seawater battery
Self-powered electrolysis
Hydrogen production
Seawater electrolysis system

ABSTRACT

Direct seawater electrolysis to sustainable production of hydrogen fuel is attractive, given the abundant seawater resource on Earth. Nevertheless, current seawater electrolysis systems necessarily require external power grid to drive the electrolysis process, which are neither able to achieve continuous hydrogen production nor applicable to mobile and undersea apparatuses. Herein, we demonstrate a self-powered, direct seawater electrolysis system driven by Mg/seawater batteries for continuous hydrogen production. For a case study, a heterostructured MoNi/$NiMoO_4$ is prepared to catalyze the hydrogen evolution reaction (HER) at the cathodes of both the Mg/seawater battery and the seawater electrolysis, displaying a superior performance surpassing a commercial Pt/C with the overpotential as low as 256 mV at 10 mA cm^{-2} in seawater. The Mg/seawater battery achieves a peak power density of 21.08 mW cm^{-2}, serving as a power source to drive seawater electrolysis. The self-powered system yields a total hydrogen evolution rate of 12.11 mL cm^{-2} h^{-1} and conversion efficiency of Mg-to-hydrogen up to 83.97%. Such a self-powered direct seawater electrolysis system provides an intriguing strategy for the continuous acquisition of hydrogen fuel from infinite seawater without any external power grids.

1. Introduction

Hydrogen has been widely considered a potential substitute for fossil fuels due to its high energy density, reproducibility, and CO_2-free emission, which is thus believed to be capable of resolving the increasingly serious energy and environment issues [1–4]. Among various hydrogen production technologies, water electrolysis has been developed as the most promising route for the continuous and efficient acquisition of hydrogen [5–7]. More meaningfully, when the water electrolysis system is directly fed with seawater, it would make full use of this unlimited natural resource while saving precious freshwater resource (<2.75% of surface water) [8–11]. However, for most of the currently developed water/seawater electrolysis systems, external power grids are necessarily required to drive the electrolysis process, which not only causes large extra electricity consumption but also creates challenges to implementation of mobile and undersea facilities [6,7,12]. Therefore, it is highly desirable to design self-powered water/seawater electrolysis systems for continuous and efficient hydrogen generation.

Various self-powered systems have been studied for electronic or electrochemical applications [13–21]. Among them, some self-powered systems have shown capability of hydrogen production [16–19,22–25]. For example, Wang and Xi et al. developed self-powered water splitting systems driven by triboelectric nanogenerator (TENG) [19,23,26]. Guo et al [27]. and Xue et al [28]. designed Zn-air batteries driven self-powered water splitting devices for hydrogen generation. To achieve uninterrupted hydrogen production, Yao et al. successfully assembled an integrated self-powered water-splitting system consisting of solar cells and Ni-Zn batteries [29]. Very recently, hydrazine fuel cells (DHzFCs) driven self-powered water/seawater electrolysis systems have also been successfully designed for hydrogen production [17,18,30]. Despite the above breakthroughs, currently reported self-powered water/seawater electrolysis systems have a few unsatisfactory characters, such as the intermittent and unstable hydrogen generation, involvement of toxic and inefficient materials, and inapplicablility for deep undersea apparatuses. Therefore, rational design of novel

* Corresponding authors.
E-mail addresses: liugb@qust.edu.cn (G. Liu), luhuajiang@qust.edu.cn (L. Jiang).
[1] These authors contributed equally to this work.

https://doi.org/10.1016/j.nanoen.2022.107295
Received 16 February 2022; Received in revised form 8 April 2022; Accepted 16 April 2022
Available online 21 April 2022

self-powered water/seawater electrolysis systems that can avoid the above drawbacks is highly desirable, yet remains challenging.

Mg/seawater batteries operating with seawater as both the electrolyte and cathodic reactant ($H_2O \rightarrow H_2 + OH^-$), can not only generate electricity but also produce hydrogen at the cathode, as illustrated in Fig. 1a. Taking advantages of an open-structured design and seawater as the electrolyte, Mg/seawater batteries are a promising power source for deep-sea apparatuses in a long-term operation. By combining a seawater battery pack with a seawater electrolyzer, as illustrated in Fig. 1b, a Mg/seawater battery driven self-powered seawater electrolysis system could be achieved, which could potentially work under deep seawater environment. More intriguingly, since hydrogen can be generated from the cathodes of both the seawater electrolyzer and the Mg/seawater battery, a high total hydrogen production rate is highly expected to obtain from this self-powered seawater electrolysis system.

Motivated by this idea with strong support of our previous works on seawater splitting and Mg/seawater batteries [31,32], herein we demonstrate a Mg/seawater battery driven self-powered direct seawater electrolysis system, which realizes continuous hydrogen production, and hold potential for mobile and undersea apparatus applications. To prove the concept of self-powered system, we constructed MoNi/$NiMoO_4$ heterostructure to catalyze the HER occurred at the cathodes of both the Mg/seawater batteries and the seawater electrolysis unit. The MoNi/$NiMoO_4$ heterostructure is rationally designed considering that the charge transfer of the HER across the interface could be facilitated by a built-in electric field established at the MoNi/$NiMoO_4$ interface benefiting from the Schottky-junction-like structure. Moreover, the formed Schottky-junction-like heterostructure could also endow the MoNi and $NiMoO_4$ surface with local electrophilic and nucleophilic regions, respectively, which is expected to greatly benefit water dissociation. As demonstrated, the MoNi/$NiMoO_4$ heterostructure electrode exhibits comparable HER in both alkaline and seawater media as compared with Pt catalysts, with a low overpotential of only 29 and 256 mV at 10 mA cm^{-2}, respectively. A Mg/seawater battery fabricated with the MoNi/$NiMoO_4$ cathode achieves a peak power density up to 21.08 mW cm^{-2}, which is among the highest performances ever reported. In particular, the designed Mg/seawater batteries drive the self-powered seawater electrolysis system with the MoNi/$NiMoO_4$ cathode to yield a high hydrogen evolution rate of 12.11 mL cm^{-2} h^{-1} and conversion efficiency of Mg-to-hydrogen up to 83.97%, which surpasses most of the state-of-the-art self-powered hydrogen production systems.

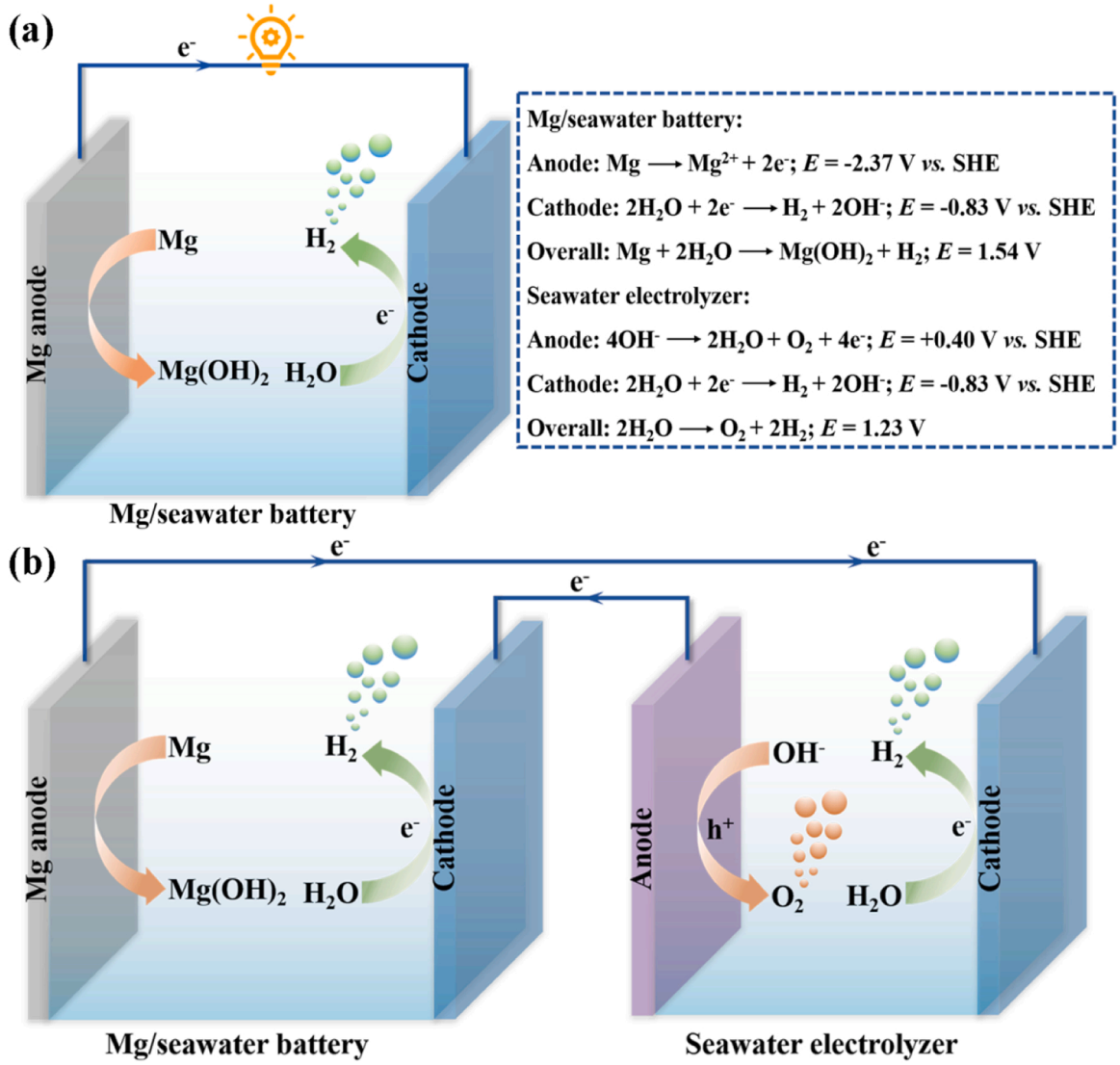

Fig. 1. (a) Illustration of the structure and working principle of the Mg/seawater battery. (b) Illustration of the Mg/seawater battery driven self-powered seawater electrolysis system.

2. Experimental methods

2.1. Synthesis of MoNi/$NiMoO_4$ electrode

$MoNi/NiMoO_4$ electrode was prepared by a hydrothermal reaction and subsequent annealing reduction strategy, as illustrated in Fig. 2a. Briefly, a commercial nickel foam (NF) substrate was cleaned by being successively washed with acetone, ethanol, 3 M HCl aqueous solution and deionized water for 15 min, and dried in vacuum for use. Then, a piece of cleaned NF (2 ×4 cm^2) was immersed in 5 mL of H_2O and 25 mL of absolute alcohol containing 0.206 g $(NH_4)_6Mo_7O_{24}.4\ H_2O$ and 0.01 g NH_4F in a Teflon-lined autoclave. Subsequently, the autoclave was heated to 150 ℃ and kept for 8 h in an oven. After cooled down to room temperature, the NF with $NiMoO_4$ precursors was obtained, which was washed with deionized water and annealed at 450 ℃ for 2 h in H_2/Ar atmosphere to obtain a NF with $MoNi/NiMoO_4$ heterostructures grown on surface. As a control experiment, $NiMoO_4$ precursors grown on NF was directly used as electrode. A Pt/NF electrode with a catalyst loading of 0.5 mg cm^{-2} was also prepared by casting the catalyst ink of 0.5 mg commercial Pt/C (20%) in 950 μL ethanol and 50 μL Nafion solution (5 wt%) on the NF (1 ×1 cm^2).

2.2. Materials characterization

X-ray diffraction (XRD) patterns were recorded on a Rigaku D-max-γ X-ray diffractometer with Cu-Kα X-ray radiation (λ = 1.5418 Å). Scanning electron microscopy (SEM) images and energy dispersive X-ray (EDX) analysis were conducted using JEOL JSM-6700 F field-emission scanning electron microscope. Transmission electron microscope (TEM) and high-resolution TEM (HRTEM) images were characterized with a JEOL JEM-2100 transmission electron microscopy. X-ray photoelectron spectroscopy (XPS) and ultraviolet photoemission spectroscopy (UPS) were performed on a Thermo Scientific ESCALab250Xi using monochromated Al Kα radiation. The UV–visible extinction spectrum was recorded on a Hitachi U-3900 UV-Vis spectrophotometer. Photoluminscence (PL) spectra were collected from a fiber optic spectrometer (Ocean Optics, QE65000) with an excitation wavelength of 435 nm.

2.3. Electrochemical characterization

The electrochemical measurements were carried out on an electrochemical workstation (CHI760E, CH Instruments, Shanghai) in a

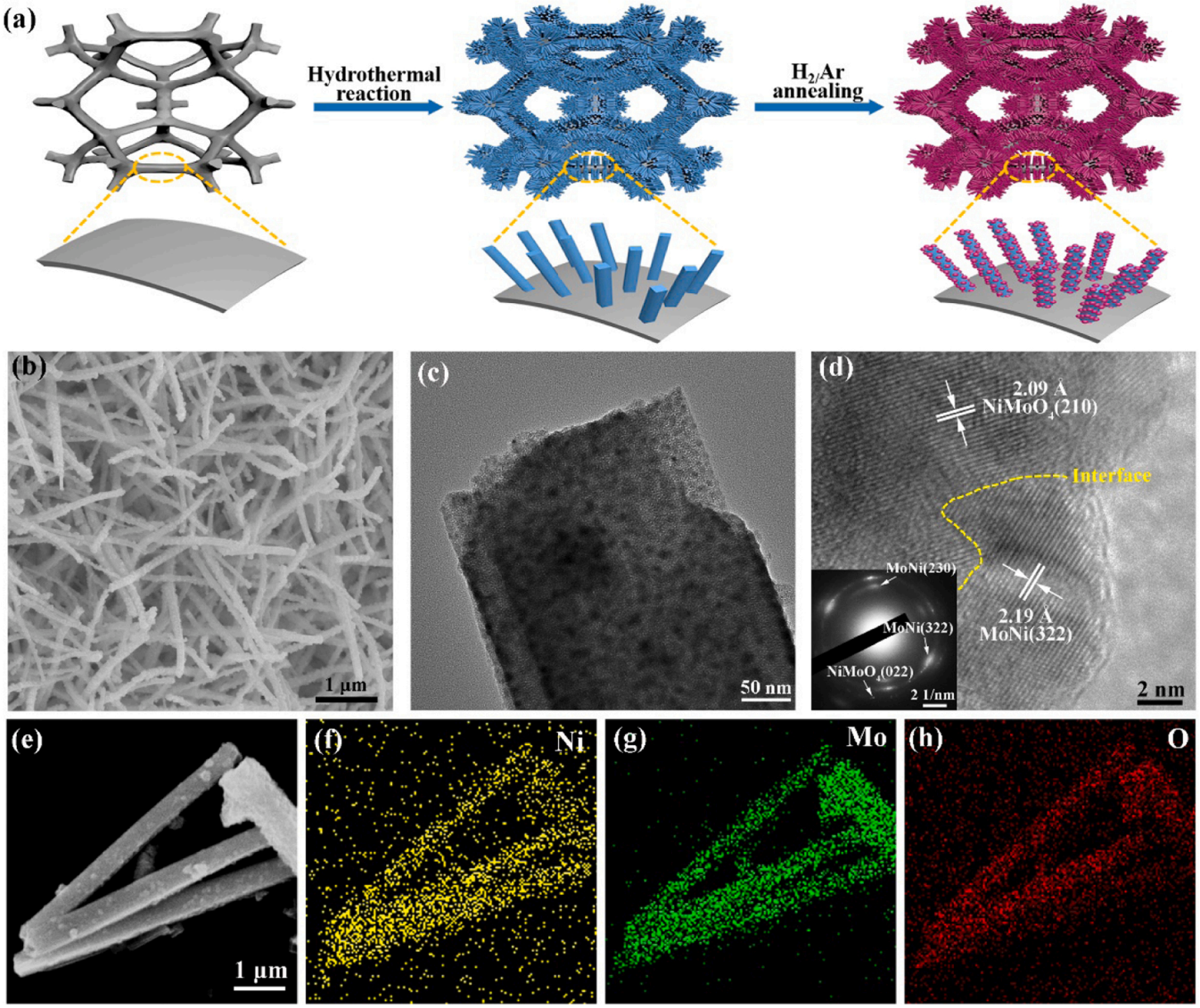

Fig. 2. (a) Schematic illustration for the synthesis of the $MoNi/NiMoO_4$ heterostructures. (b) SEM, (c) TEM and (d) HRTEM images and the SAED patterns of $MoNi/NiMoO_4$ heterostructures. (e) SEM image and (f-h) corresponding EDX elemental mappings of the $MoNi/NiMoO_4$ heterostructures.

conventional three-electrode system. The as-prepared NF sheet with MoNi/$NiMoO_4$ on surface was used as working electrode with 1.0 M KOH solution or simulated seawater (0.5 M NaCl) as the electrolytes. A saturated calomel electrode (SCE) and a Hg/HgO electrode were served as the reference electrode in seawater and 1 M KOH, respectively. All potentials were *iR*-corrected and converted to potential vs. reversible hydrogen electrode (RHE). The linear sweep voltammetry (LSV) curves were recorded at a scan rate of 5 mV s^{-1} in electrolytes after saturation with N_2 for 30 min. The electrochemical impedance spectroscopy (EIS) was carried out at the open circuit voltage with a frequency range of 100 kHz-100 mHz. The capacitances of the double layer (C_{dl}) were fitted by measuring the CVs in the potential window without faradic processes at scan rates of 20, 40, 60, 80, 100 mV s^{-1}. Photocurrent measurement was obtained at the bias potential of 0 V vs. RHE under irradiation of a 500 W Xe lamp fitted with light intensity of 100 mW cm^{-2}.

2.4. Fabrication and tests of the Mg/seawater battery and self-powered seawater electrolysis system

For convenience in this work, the electrode occurring reduction reaction is denoted as cathode and oxidation reaction as anode for both battery and electrolyzer. The Mg/seawater battery was fabricated using a homemade flow cell with MoNi/$NiMoO_4$ grown on NF as the cathode, a Mg alloy sheet (AZ31) as the anode, and simulated seawater (0.5 M NaCl) as the electrolyte. Both the anode and cathode electrodes have a working area of 5 cm^2, and the electrode distance was 2 mm. A seawater electrolysis system was fabricated using a water electrolysis apparatus with MoNi/$NiMoO_4$ grown on NF as the cathode, commercial Ir/C loaded on NF as the anode, and alkaline seawater (1 M KOH + 0.5 M NaCl) or natural seawater (pH 8.2) as the electrolyte. For natural seawater, it was collected from the Yellow Sea (Qingdao, China) and filtered to remove visible impurities before use. The self-powered seawater electrolysis system was built by combining the seawater electrolysis system with a Mg/seawater battery pack. The Mg/seawater battery performance was evaluated using a battery testing system (CT-4008–5V6A-S1-F, Neware Company). The volume of the produced hydrogen was measured by the drainage method.

3. Results and discussion

3.1. Synthesis and characterization of the MoNi/$NiMoO_4$ heterostructures

The MoNi/$NiMoO_4$ heterostructures were prepared according to the synthetic route illustrated in Fig. 2a. Firstly, $NiMoO_4{\cdot}xH_2O$ precursors were prepared by a hydrothermal method. Then, the $NiMoO_4{\cdot}xH_2O$ precursors were subsequently annealed under H_2/Ar atmosphere at 450 ℃ for 2 h to obtain the MoNi/$NiMoO_4$ heterostructures. XRD data indicate that the hydrothermal product can be well assigned to the $NiMoO_4{\cdot}xH_2O$ (JCPDS No.13–0128, Fig. S1). After annealing in reducing atmosphere (H_2/Ar), orthorhombic MoNi (JCPDS No.65–6903) and monoclinic $NiMoO_4$ (JCPDS No.86–0362, Fig. S1) appeared, as confirmed by the XRD pattern in Fig. S1, suggesting the successful transformation of $NiMoO_4{\cdot}xH_2O$ into MoNi/$NiMoO_4$ composite. SEM images (Fig. S2) indicate that the $NiMoO_4{\cdot}xH_2O$ precursors are vertically grown on the NF and display a nanorod morphology with smooth surface. By contrast, the MoNi/$NiMoO_4$ composites demonstrate the similar nanorod morphology, but with much rougher surface, as shown in Fig. 1b. TEM was performed to further investigate the detailed structure of the MoNi/$NiMoO_4$ composite. As shown the TEM image (Fig. 1c), most nanoparticles with sizes of 5–10 nm can be observed anchoring on the surface of the nanorod. In the HRTEM image (Fig. 1d), the crystal lattice fringes reveal interplanar spacing of 2.19 Å, corresponding to the (322) planes of MoNi alloy, indicating these nanoparticles are MoNi nanocrystals. These lattice fringes with interplanar spacing of 2.09 Å can be assigned to the (210) planes of $NiMoO_4$. Meanwhile, it can be observed that the MoNi alloy and $NiMoO_4$ semiconductor have formed an intimate contact but with a clear interface between them, indicating the formation of the MoNi/$NiMoO_4$ heterostructures. In addition, selected area electron diffraction (SAED) patterns (inset in Fig. 1d) further confirm the coexistence of the MoNi and $NiMoO_4$ phases, which is in accordance with the HRTEM and XRD results. Moreover, as shown Fig. 1e-h, EDX analysis verifies that Mo, Ni and O elements are uniformly distributed in the entire MoNi/$NiMoO_4$ nanorods, suggesting the formed MoNi/$NiMoO_4$ heterostructures are ultrafine and sufficiently exposed on the surface.

Furthermore, the surface composition and chemical valence states of parent $NiMoO_4$ and MoNi/$NiMoO_4$ composites were investigated by XPS. The survey XPS spectra show obvious characteristic peaks of Mo, Ni and O in all the investigated samples (Fig. S3), confirming these component elements. Fig. 3a and b show the high-resolution Mo 3d and Ni 2p spectra of $NiMoO_4$ and MoNi/$NiMoO_4$, respectively. For $NiMoO_4$, the Mo 3d spectrum (Fig. 3a) displays two peaks at 231.9 eV (Mo^{6+} $3d_{5/2}$) and 235.1 eV (Mo^{6+} $3d_{3/2}$) [33,34], and the Ni 2p spectrum (Fig. 3b) displays two groups of spin-orbit peaks, that is, two peaks at 855.7 eV (Ni^{2+} $2p_{3/2}$), 873.4 eV (Ni^{2+} $2p_{1/2}$) and the two satellite peaks at 861.3 eV and 879.4 eV [35]. For MoNi/$NiMoO_4$, in addition to the peaks corresponding to Mo^{6+} and Ni^{2+}, new peaks corresponding to Mo^{5+} (230.2/233.4 eV), Mo^{4+} (228.9/232.1 eV), Mo^0 (227.8/231.1 eV), and Ni^0 (852.3/869.5 eV) are observed [35,36]. Note that, the peaks of Mo^0 and Ni^0 confirm the formation of metallic MoNi alloy, which is consistent with the TEM and XRD results. Additionally, the peaks of Mo^{5+} and Mo^{4+} indicate the existence of abundant oxygen vacancies in the MoNi/$NiMoO_4$ composite, as verified by the appeared peak at 531.4 eV in its O 1 s spectrum (Fig. 3c) [37].

To investigate the interfacial interactions and energy band diagrams of the MoNi/$NiMoO_4$ heterostructure, UPS and UV–visible extinction spectra of MoNi and $NiMoO_4$ were collected (Fig. 3d and Fig. S4). As shown in Fig. 3d, the UPS spectra indicate that the secondary electron cutoff point (E_{cutoff}) of MoNi and $NiMoO_4$ is 17.90 and 17.51 eV, respectively. The work function (Φ) is thus determined to be 3.32 eV for MoNi and 3.71 eV for $NiMoO_4$, respectively, according to the formula $\Phi = h\nu - E_{cutoff} + E_F$ [38], where the $h\nu$ = 21.22 eV, E_F = 0 eV in our case. Since the work functions of MoNi is lower than that of $NiMoO_4$ (Fig. 3e), electrons can flow from MoNi to $NiMoO_4$ across the interface of MoNi/$NiMoO_4$ to achieve an equilibrium, thus resulting in the band bending and Schottky barrier (Fig. 3f). This can lead to a built-in electric field at the MoNi/$NiMoO_4$ Schottky interface, which could significantly promote the charge separation/transportation and electrode kinetics [39,40]. This is also supported by the much quenched PL intensity and high photocurrent density of MoNi/$NiMoO_4$ as compared with pure $NiMoO_4$ (Fig. S5). Therefore, the above results reveal that MoNi/$NiMoO_4$ heterostructures with Schottky-junction-like interfaces have been successfully constructed.

3.2. Electrochemical HER performance of the MoNi/$NiMoO_4$ heterostructures

High HER activity is of great importance for a Mg/seawater battery, which would guarantee low cathodic polarization during discharging and thus high overall battery performance. Therefore, we evaluated the HER activities of MoNi/$NiMoO_4$ heterostructures in both 1.0 M KOH and simulated seawater. The MoNi/$NiMoO_4$ heterostructures prepared with different annealing temperatures (350, 450, and 550 ℃) were firstly evaluated in 1.0 M KOH by LSV measurements. The results in Fig. S6 show that the MoNi/$NiMoO_4$ heterostructures treated under 450 ℃ achieved the best HER activity. Therefore, 450 ℃ was chosen as the annealing temperature to prepare the MoNi/$NiMoO_4$ heterostructures. In addition, blank NF, $NiMoO_4$ precursor, and commercial Pt/C (20 wt%) were also evaluated for comparison. Fig. 4a and d represent the LSV curves in 1.0 M KOH and simulated seawater for all the tested samples. As can be seen, the HER occurred on blank NF and

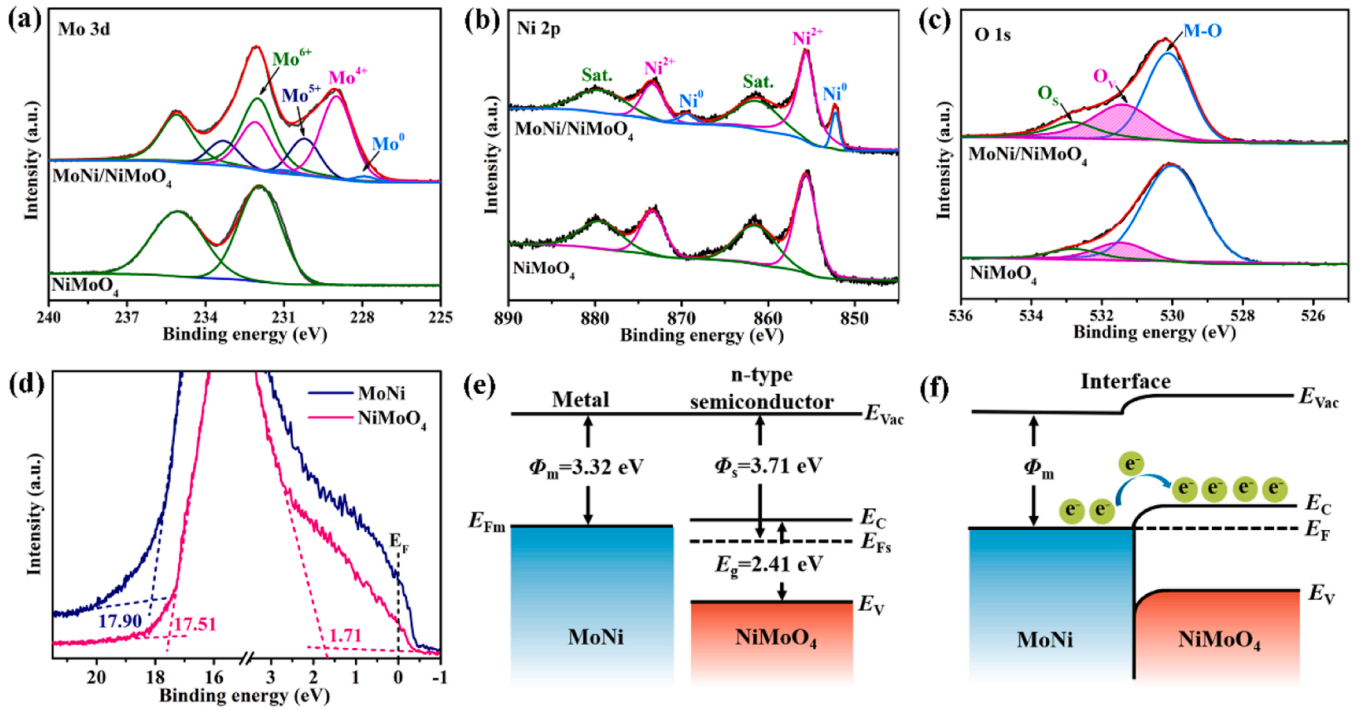

Fig. 3. High resolution XPS spectra of (a) Mo 3d (b) Ni 2p, (c) O 1 s for $NiMoO_4$ and MoNi/$NiMoO_4$ heterostructures. (d) UPS analysis of MoNi and $NiMoO_4$. Energy band diagrams of MoNi alloy and $NiMoO_4$ semiconductor (e) before and (f) after contact. (E_{Vac} = vacuum energy, Φ = work function, E_F = Fermi level, E_C = conduction band, E_V = valence band, E_g = band gap).

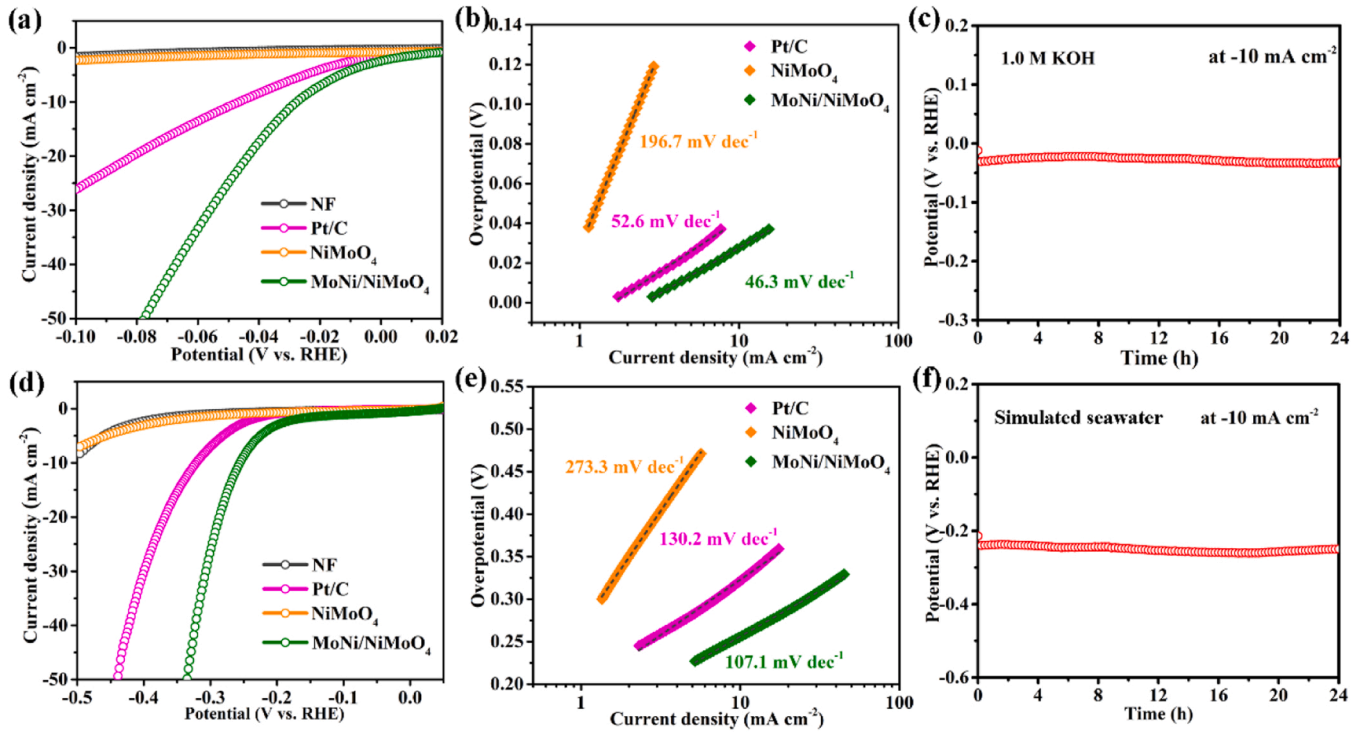

Fig. 4. HER performance of electrocatalysts in (a-c) 1.0 M KOH and (d-f) simulated seawater. (a, d) linear scanning voltammogram curves, (b, e) Tafel plots and (c, f) the HER stability test of the MoNi/$NiMoO_4$ catalyst in simulated seawater.

$NiMoO_4$ precursor demonstrate very high overpotentials, indicating the poor HER activity. Remarkably, the MoNi/$NiMoO_4$ heterostructures exhibit an overpotential of only 29 and 256 mV to obtain the current density of 10 mA cm^{-2} in 1.0 M KOH and simulated seawater, respectively. Interestingly, the HER performance of MoNi/$NiMoO_4$ heterostructures is superior to that of the Pt/C catalyst that requires an overpotential of 47 and 322 mV to obtain the current density of 10 mA cm^{-2} in 1.0 M KOH and simulated seawater, respectively, indicating the excellent HER activity can be achieved on the heterostructures. It is worth mentioning that, the superior HER activity of the

MoNi/$NiMoO_4$ heterostructures in seawater outperforms most of the state-of-the-art HER electrocatalysts investigated in seawater media, like Ni-MoO_2 (412 mV) [31], CoP/Co_2P (454 mV) [32], CoMoP@C (450 mV) [41], and Mo_2C-MoP (346 mV) [42] (see Table S1 for details). The remarkable HER activity of the MoNi/$NiMoO_4$ heterostructures is embodied by the Tafel plots. As shown in Fig. 4b and e, the Tafel slope of MoNi/$NiMoO_4$ heterostructures is 46.3 and 107 mV dec^{-1} in alkaline and seawater media, respectively, which is much lower than that of the $NiMoO_4$ and commercial Pt/C, indicating more favorable HER kinetics. Since the Tafel plots are in the theoretical value range of 40–120 mV dec^{-1}, suggesting the HER on the MoNi/$NiMoO_4$ heterostructures follows a Volmer-Heyrovsky mechanism in alkaline and seawater media [32]. Furthermore, the stability of MoNi/$NiMoO_4$ heterostructures was examined at the current density of 10 mA cm^{-2} using chronopotentiometry test. Fig. 4c and f shows the chronopotentiometric curves recorded in 1.0 M KOH and simulated seawater, respectively, which demonstrate no obvious degradation during long term electrocatalytic process of 24 h, indicating the excellent stability. SEM image and XPS characterizations show that the main composition and phase of MoNi/$NiMoO_4$ heterostructures are well maintained after 24 h operation in simulated seawater (Fig. S7 and S8), confirming the stability of the MoNi/$NiMoO_4$ heterostructures in seawater medium.

To probe the origin of the superior HER activity of MoNi/$NiMoO_4$ heterostructures, electrochemical double-layer capacitance (C_{dl}) was performed to evaluate the electrochemical surface area (ECSA). It turned out that MoNi/$NiMoO_4$ heterostructures demonstrate large C_{dl} of 281.6 and 110.5 mF cm^{-2} in alkaline and seawater media, respectively, which is over 23 times and 8 times higher than that of the $NiMoO_4$ precursor (Fig. S9). This indicates that the MoNi/$NiMoO_4$ heterostructures possess much more exposed active sites and enhanced anion accessibility for HER, which probably stem from the abundant interfaces and oxygen vacancies existed in the heterostructures. Additionally, to evaluate the intrinsic activity of catalysts, the values of exchange current density (j_0) on various catalysts were calculated by extrapolating the Tafel plots in 1.0 M KOH. As shown in Fig. S10, the j_0 value of MoNi/$NiMoO_4$ heterostructures is 2.57 mA cm^{-2}, which is much larger than that of the $NiMoO_4$ (0.72 mA cm^{-2}) and commercial Pt/C (1.62 mA cm^{-2}), corroborating the high intrinsic activity. To gain deep insights into the HER kinetics of the samples, EIS measurement was performed in 1.0 M KOH and simulated seawater. Fig. S11 shows the Nyquist plots which reflect the solution resistance (R_s) and charge transfer resistances (R_{ct}). Obviously, with MoNi/$NiMoO_4$ heterostructures, the R_s and R_{ct} are much lower than with $NiMoO_4$, indicating the more rapid electron transfer and thus faster kinetics for HER with the former.

Based on the above experimental results, the excellent HER performance in both alkaline and seawater media for MoNi/$NiMoO_4$ heterostructures can be attributed to the following aspects: (i) the three-dimensional NF substrate guarantees large ECSA, abundant active sites, and facile release of generated gas bubbles (Fig. 2b and Fig. S9); (ii) the Schottky-junction effect between MoNi alloy and $NiMoO_4$ semiconductor not only significantly promotes the charge separation/transportation (Fig. S5), but also greatly endows the MoNi and $NiMoO_4$ surface with local electrophilic and nucleophilic region, and thus accelerating the water dissociation and electrode kinetics (Fig. 4b and e); (iii) the abundant interfaces and oxygen vacancies existed in the MoNi/$NiMoO_4$ heterostructures provide additional active sites and enhance the electrical conductivity and electron transfer for HER (Fig. 2c, Fig. 3c and Fig. S11).

3.3. Evaluation of Mg/seawater battery with a MoNi/$NiMoO_4$ heterostructure cathode

Given the excellent HER activity of MoNi/$NiMoO_4$ heterostructures in simulated seawater, we further demonstrate its practical application in Mg/seawater batteries. To this end, we assembled a Mg/seawater battery with MoNi/$NiMoO_4$ heterostructures as the cathode, a Mg alloy sheet (AZ31) as the anode, and simulated seawater as the electrolyte. For comparison, the Mg/seawater battery assembled with a blank NF cathode, a $NiMoO_4$ cathode or a commercial Pt/C catalyst cathode, respectively, were also evaluated. The recorded discharging curve and the corresponding power density curve of the as-assembled Mg/seawater battery are presented in Fig. 5a. The open circuit voltages (OCVs) for Mg/seawater battery with different cathodes reach up to 1.18–1.56 V. The ultrahigh OCVs are believed to be attributed to the existence of dissolved oxygen in the electrolyte, which drop rapidly as the dissolved oxygen is consumed [43]. Then, with the discharging current density increasing the discharging voltage decreases linearly. From the corresponding power density curves, we can see that the as-assembled Mg/seawater battery with the MoNi/$NiMoO_4$ heterostructures cathode exhibits a maximum output power density up to 21.08 mW cm^{-2}, which is much superior to that of the Mg/seawater batteries with the blank NF cathode (2.91 mW cm^{-2}), the $NiMoO_4$ cathode (3.32 mW cm^{-2}) and the commercial Pt/C cathode (12.9 mW cm^{-2}). Of note, this value is among the best performances of Mg/seawater batteries ever reported (see details in Table S2, Supporting Information) [31,32,43,44]. Moreover, Fig. 5b shows the long-term discharging ability of the Mg/seawater battery with MoNi/$NiMoO_4$ heterostructures cathode under galvanostatic discharging at 3 mA cm^{-2} for 100 h. As seen, the output voltage of the Mg/seawater battery stabilizes in the range from 0.61 to 0.54 V during the 100 h discharging, indicating the excellent stability, which is consistent with the outstanding long-term half-cell HER performance in seawater media (Fig. 4f). To demonstrate the applicability for the energy supply in practice devices, a Mg/seawater battery pack was assembled by connecting four Mg/seawater single batteries with MoNi/$NiMoO_4$ heterostructure cathodes together in series. Fig. 5c shows an illustration of the assembled Mg/seawater battery pack, which exhibits a high OCV of 2.32 V. Moreover, as presented in Fig. 5d, the as-assembled Mg/seawater battery pack is able to power the light-emitting diode (LED) display screen, suggesting its potential practical applications.

3.4. Demonstration of Mg/seawater battery driven self-powered seawater electrolysis system

Inspired by the excellent Mg/seawater battery performance, we further demonstrate the potential application in seawater electrolysis for hydrogen production. Since both the Mg/seawater battery and seawater electrolysis system involve a HER cathode and seawater electrolyte, it is highly intriguing to integrate them together, thus achieving efficient acquisition of hydrogen from seawater. Therefore, as a proof-of-concept, we constructed a Mg/seawater battery pack driven self-powered seawater electrolysis system, which contains a Mg/seawater battery pack, alkaline seawater electrolyzer, and gas collection setups for collecting the hydrogen generated from the HER cathodes of alkaline seawater electrolyzer and Mg/seawater batteries. Fig. 6a shows the photograph of our constructed Mg/seawater battery driven self-powered seawater electrolysis system. As seen in Movie S1 and S2 (Supporting Information), continuous bubbling can be clearly observed under working conditions, suggesting the feasibility of the developed system for real-time and continuous hydrogen generation from seawater. To evaluate the hydrogen yield of the whole system, the volumes of hydrogen generated from the Mg/seawater battery and the cathode of seawater electrolyzer were recorded at different time, as shown in Fig. 6b and c. Then the hydrogen production rate per unit area of the HER cathode was calculated. The final results are presented in Fig. 6d, from which a linear scaling can be observed between the hydrogen yield and time. It is calculated that the hydrogen production rate for the Mg/seawater battery and cathode of seawater electrolyzer is 3.52 and 8.59 mL cm^{-2} h^{-1}, respectively, resulting in a total hydrogen production rate of the integrated system up to 12.11 mL cm^{-2} h^{-1}, which is highly competitive among those state-of-the-art self-powered hydrogen production systems [16,28,29,45–47].

Supplementary material related to this article can be found online at

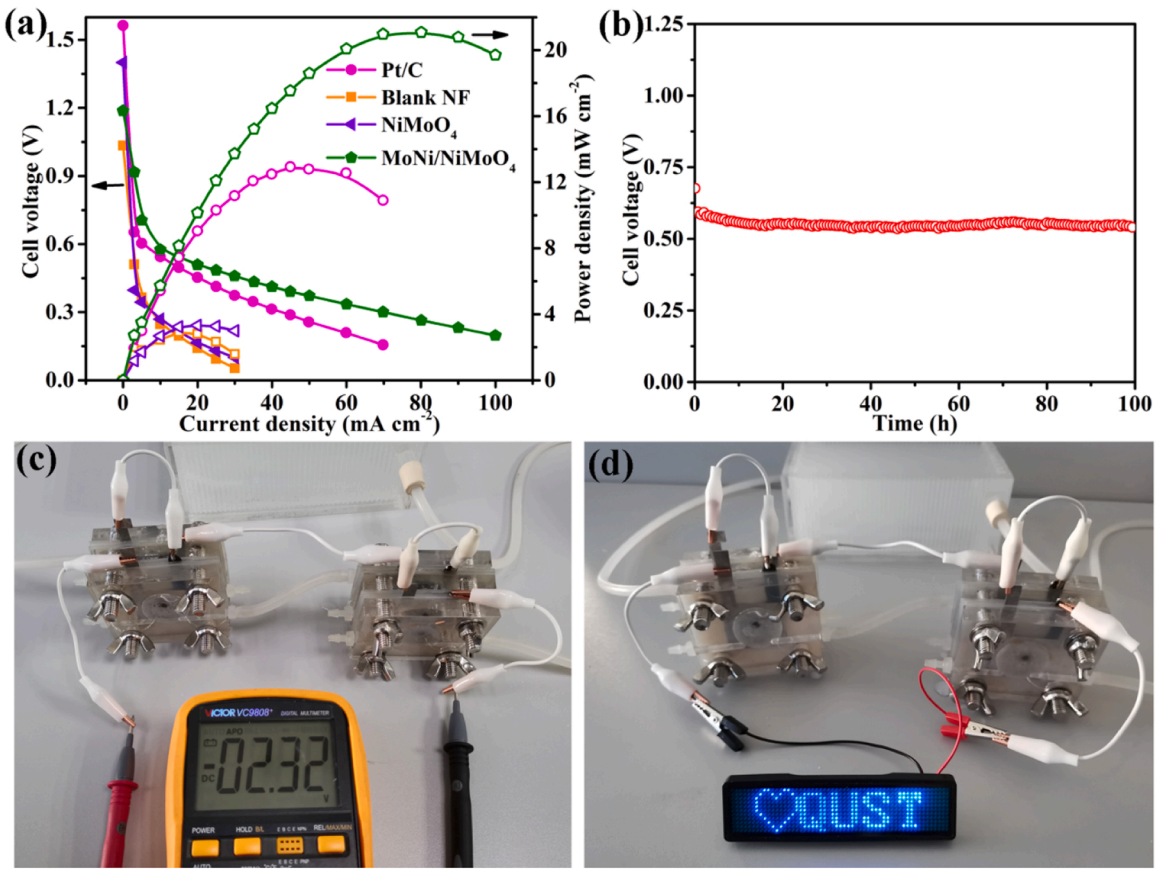

Fig. 5. (a) Discharging curves and the corresponding power density curves of the Mg/seawater battery with various cathodes. (b) Stability test of the Mg/seawater battery with a MoNi/$NiMoO_4$ heterostructures cathode at the current density of 3 mA cm^{-2}. (c) Open circuit voltage of the as-fabricated Mg/seawater battery pack with MoNi/$NiMoO_4$ heterostructure cathodes. (d) Photograph of a LED display screen powered by the Mg/seawater battery pack with MoNi/$NiMoO_4$ heterostructure cathodes.

doi:10.1016/j.nanoen.2022.107295.

To better understand the performance parameters of the novel system, the conversion efficiency (CE) of Mg-to-hydrogen was carried out according to the following equation:

$$CE = \frac{\text{Moles of generated } H_2}{\text{Moles of consumed Mg}} \times 100\% = \frac{V/V_m}{(m_0\text{-}m)/M} \times 100\%$$

where, V is the volume of collected H_2, V_m is the molar volume of gases, m_0 and m is the Mg anode weight before and after discharging, respectively, and M is the molar weight of Mg. According to the above equation, with a given Mg anode, a high hydrogen generation rate corresponds a high CE, meaning the cathodes of the self-powered seawater electrolysis system showed a high HER activity. In our case, the CE of the as-developed system is up to 83.97%, confirming the high HER activity of the MoNi/$NiMoO_4$ heterostructure cathodes. To get a thorough understanding of the system, we further evaluate the performance of the self-powered seawater electrolysis system with natural seawater (see Fig. S12). It turned out that the total hydrogen evolution rate and CE of the system are calculated to be 9.28 mL cm^{-2} h^{-1} and 68.16%, respectively, which are lower than that of the system with alkaline seawater, due to the inferior HER and battery performance of MoNi/$NiMoO_4$ cathode in natural seawater (see Fig. S13). It is easy to understand that with real seawater, the HER kinetics is rather slow due to the lack of protons or hydroxyl ions, on the other hand, the dissolved cations (Mg^{2+}, Ca^2, and etc.), bacteria/microbes and small particulates could inevitably cause cathode blocking and corrosion [8,10], all of which result in the poor battery and HER performances and thus the low hydrogen evolution rate and CE of the whole system. However, it is believed that these adverse substances could be effectively relieved by vast mass of flowing seawater under real undersea environment, thus a better performance could be expected for the system.

Overall, whether compared with the state-of-the-art hydrogen storage technologies or self-powered hydrogen production systems, our newly developed system takes three significant advantages: (i) it can act as an instant hydrogen production technology, which thus can save the cost of storage and transportation in hydrogen utilizations; (ii) it can realize continuous production of high-purity hydrogen from the in-situ seawater without any external power supplies, which has potential applications in mobile and even undersea apparatuses; (iii) it can work under normal temperature and pressure, and the whole process only consumes seawater and Mg resources, which is completely recyclable and environmentally friendly. Therefore, our strategy is of great importance for multiple industrial and military applications.

4. Conclusions

In summary, we successfully developed a Mg/seawater battery driven, self-powered seawater electrolysis system for hydrogen production based on a MoNi/$NiMoO_4$ heterostructure cathode. The MoNi/$NiMoO_4$ heterostructure electrodes exhibited excellent half-cell HER performance with overpotential of only 29 and 256 mV at 10 mA cm^{-2} in alkaline and seawater media, respectively. A Mg/seawater battery coupling with MoNi/$NiMoO_4$ heterostructure cathode achieved a peak power density up to 21.08 mW cm^{-2}, which is the best Mg/seawater battery performance ever reported. In particularly, the designed Mg/seawater batteries driven self-powered seawater electrolysis system yielded a total hydrogen evolution rate of 12.11 mL cm^{-2} h^{-1} and

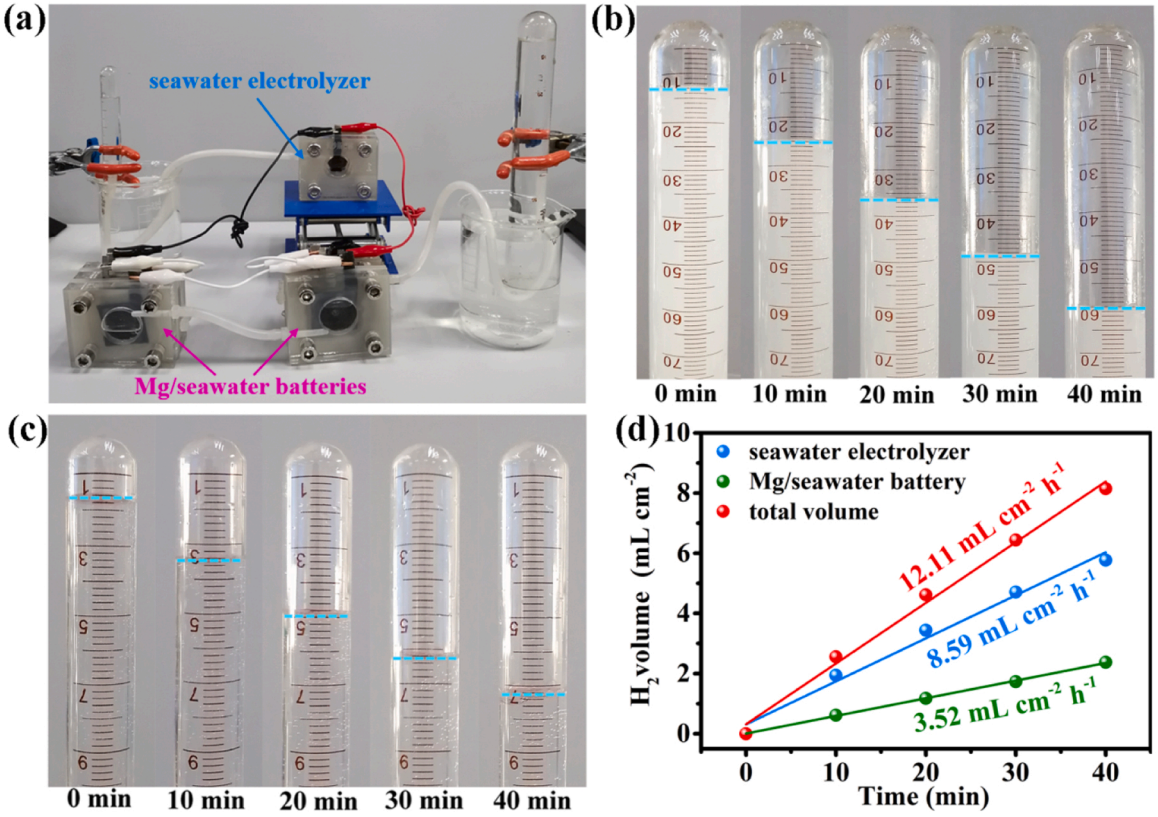

Fig. 6. (a) Photograph of the as-assembled Mg/seawater battery driven self-powered seawater electrolysis system. Photographs of the gas collection tubes at different time connected with (b) the Mg/seawater battery pack and (c) the cathode of the seawater electrolyzer. (d) The hydrogen production rates for the Mg/seawater battery driven self-powered seawater electrolysis system.

conversion efficiency of Mg-to-hydrogen up to 83.97%. This work provides an innovative and efficient route to real-time acquisition of hydrogen from seawater without any external power grids, thus holding great promise for the efficient conversion and utilization of the infinite seawater resource.

CRediT authorship contribution statement

Yingshuang Xu: Investigation, Data Curation, Writing – original draft. **Honghao Lv:** Investigation, Data curation, Discussion. **Huasen Lu:** Visualization, Software, Investigation. **Qinghao Quan:** Validation, Investigation. **Wenzhen Li:** Discussion, Writing – review and editing. **Xuejing Cui:** Resources, Funding acquisition. **Guangbo Liu:** Conceptualization, Methodology, Discussion, Writing – review and editing. **Luhua Jiang:** Conceptualization, Supervision, Funding acquisition, Writing – review and editing.

Declaration of Competing Interest

The authors declare that they have no known competing financial interests or personal relationships that could have appeared to influence the work reported in this paper.

Acknowledgments

This work was financially supported by National Natural Science Foundation of China (22179067), Natural Science Foundation of Shandong Province (ZR2020MB025) and Taishan Scholar Program of Shandong Province (ts201712046). The authors also appreciate Hengzhou Liu at Iowa State University for reviewing and giving some valuable suggestions on this work.

Appendix A. Supporting information

Supplementary data associated with this article can be found in the online version at doi:10.1016/j.nanoen.2022.107295.

References

[1] I. Staffell, D. Scamman, A. Velazquez Abad, P. Balcombe, P.E. Dodds, P. Ekins, N. Shah, K.R. Ward, The role of hydrogen and fuel cells in the global energy system, Energy Environ. Sci. 12 (2019) 463–491.
[2] M.S. Dresselhaus, I.L. Thomas, Alternative energy technologies, Nature 414 (2001) 332–337.
[3] J.A. Turner, Sustainable hydrogen production, Science 305 (2004) 972–974.
[4] T.-Y. Jeon, S.-H. Yu, S.J. Yoo, H.-Y. Park, S.-K. Kim, Electrochemical determination of the degree of atomic surface roughness in Pt-Ni alloy nanocatalysts for oxygen reduction reaction, Carbon Energy 3 (2021) 375–383.
[5] X. Qin, D. Kim, Y. Piao, Metal-organic frameworks-derived novel nanostructured electrocatalysts for oxygen evolution reaction, Carbon Energy 3 (2021) 66–100.
[6] Z.Y. Yu, Y. Duan, X.Y. Feng, X.X. Yu, M.R. Gao, S.H. Yu, Clean and affordable hydrogen fuel from alkaline water splitting: past, recent progress, and future prospects, Adv. Mater. 33 (2021), 2007100.
[7] J. Wang, Y. Gao, H. Kong, J. Kim, S. Choi, F. Ciucci, Y. Hao, S.H. Yang, Z.P. Shao, J. Lim, Non-precious-metal catalysts for alkaline water electrolysis: operando characterizations, theoretical calculations, and recent advances, Chem. Soc. Rev. 49 (2020) 9154–9196.
[8] W. Tong, M. Forster, F. Dionigi, S. Dresp, R. Sadeghi Erami, P. Strasser, A.J. Cowan, P. Farràs, Electrolysis of low-grade and saline surface water, Nat. Energy 5 (2020) 367–377.
[9] G. Liu, Y. Xu, T. Yang, L. Jiang, Recent advances in electrocatalysts for seawater splitting, Nano Mater. Sci. (2020), https://doi.org/10.1016/j.nanoms.2020.1012.1003.
[10] S. Dresp, F. Dionigi, M. Klingenhof, P. Strasser, Direct electrolytic splitting of seawater: opportunities and challenges, ACS Energy Lett. 4 (2019) 933–942.
[11] M. Chung, K. Jin, J.S. Zeng, K. Manthiram, Mechanism of chlorine-mediated electrochemical ethylene oxidation in saline water, ACS Catal. 10 (2020) 14015–14023.
[12] C.L. Hu, L. Zhang, J.L. Gong, Recent progress made in the mechanism comprehension and design of electrocatalysts for alkaline water splitting, Energy Environ. Sci. 12 (2019) 2620–2645.

[13] Q. Jiang, Y. Han, W. Tang, H. Zhu, C. Gao, S. Chen, M. Willander, X. Cao, Z. Lin, Wang, Self-powered seawater desalination and electrolysis using flowing kinetic energy, Nano Energy 15 (2015) 266–274.
[14] Q. Zheng, Q.Z. Tang, Z.L. Wang, Z. Li, Self-powered cardiovascular electronic devices and systems, Nat. Rev. Cardiol. 18 (2021) 7–21.
[15] J. Chen, H. Guo, Z. Wu, G. Xu, Y. Zi, C. Hu, Z.L. Wang, Actuation and sensor integrated self-powered cantilever system based on TENG technology, Nano Energy 64 (2019), 103920.
[16] N. Zhai, Z. Wen, X. Chen, A. Wei, M. Sha, J. Fu, Y. Liu, J. Zhong, X. Sun, Blue energy collection toward all-hours self-powered chemical energy conversion, Adv. Energy Mater. 10 (2020), 2001041.
[17] Y. Liu, J. Zhang, Y. Li, Q. Qian, Z. Li, Y. Zhu, G. Zhang, Manipulating dehydrogenation kinetics through dual-doping Co_3N electrode enables highly efficient hydrazine oxidation assisting self-powered H_2 production, Nat. Commun. 11 (2020) 1853.
[18] X. Liu, J. He, S. Zhao, Y. Liu, Z. Zhao, J. Luo, G. Hu, X. Sun, Y. Ding, Self-powered H_2 production with bifunctional hydrazine as sole consumable, Nat. Commun. 9 (2018) 4365.
[19] W. Tang, Y. Han, C.B. Han, C.Z. Gao, X. Cao, Z.L. Wang, Self-powered water splitting using flowing kinetic energy, Adv. Mater. 27 (2015) 272–276.
[20] Y. Han, W. Wang, J. Zou, Z. Li, X. Cao, S. Xu, Self-powered energy conversion and energy storage system based on triboelectric nanogenerator, Nano Energy 76 (2020), 105008.
[21] H. Yang, M. Wang, M. Deng, H. Guo, W. Zhang, H. Yang, Y. Xi, X. Li, C. Hu, Z. Wang, A full-packaged rolling triboelectric-electromagnetic hybrid nanogenerator for energy harvesting and building up self-powered wireless systems, Nano Energy 56 (2019) 300–306.
[22] J. Yang, X. Wang, B. Li, L. Ma, L. Shi, Y. Xiong, H. Xu, Novel iron/cobalt-containing polypyrrole hydrogel-derived trifunctional electrocatalyst for self-powered overall water splitting, Adv. Funct. Mater. 27 (2017), 1606497.
[23] Y. Yang, H. Zhang, Z.-H. Lin, Y. Liu, J. Chen, Z. Lin, Y.S. Zhou, C.P. Wong, Z. L. Wang, A hybrid energy cell for self-powered water splitting, Energy Environ. Sci. 6 (2013) 2429–2434.
[24] Z. Bai, S. Li, J. Fu, Q. Zhang, F. Chang, L. Yang, J. Lu, Z. Chen, Metal-organic framework-derived Nickel Cobalt oxysulfide nanocages as trifunctional electrocatalysts for high efficiency power to hydrogen, Nano Energy 58 (2019) 680–686.
[25] Y. Wu, Z. Tian, S. Yuan, Z. Qi, Y. Feng, Y. Wang, R. Huang, Y. Zhao, J. Sun, W. Zhao, W. Guo, J. Feng, J. Sun, Solar-driven self-powered alkaline seawater electrolysis via multifunctional earth-abundant heterostructures, Chem. Eng. J. 411 (2021), 128538.
[26] H. Yang, M. Deng, Q. Zeng, X. Zhang, J. Hu, Q. Tang, H. Yang, C. Hu, Y. Xi, Z. L. Wang, Polydirectional microvibration energy collection for self-powered multifunctional systems based on hybridized nanogenerators, ACS Nano 14 (2020) 3328–3336.
[27] J. Yin, Y. Li, F. Lv, M. Lu, K. Sun, W. Wang, L. Wang, F. Cheng, Y. Li, P. Xi, S. Guo, Oxygen vacancies dominated NiS_2/CoS_2 interface porous nanowires for portable Zn-air batteries driven water splitting devices, Adv. Mater. 29 (2017), 1704681.
[28] P. Liu, D. Gao, W. Xiao, L. Ma, K. Sun, P. Xi, D. Xue, J. Wang, Self-powered water-splitting devices by core-shell NiFe@N-graphite-based Zn-air batteries, Adv. Funct. Mater. 28 (2018), 1706928.
[29] Q. Zhang, B. He, L. Tang, Z. Zhou, L. Kang, J. Sun, T. Zhang, Q. Li, C. Li, J. Zhao, Z. Zhang, L. Wei, Y. Yao, Fully Solar-powered uninterrupted overall water-splitting systems, Adv. Funct. Mater. 29 (2019), 1808889.
[30] F. Sun, J. Qin, Z. Wang, M. Yu, X. Wu, X. Sun, J. Qiu, Energy-saving hydrogen production by chlorine-free hybrid seawater splitting coupling hydrazine degradation, Nat. Commun. 12 (2021) 4182.
[31] T. Yang, Y. Xu, H. Lv, M. Wang, X. Cui, G. Liu, L. Jiang, Triggering the intrinsic catalytic activity of Ni-doped molybdenum oxides via phase engineering for hydrogen evolution and application in Mg/seawater batteries, ACS Sustain. Chem. Eng. 9 (2021) 13106–13113.
[32] G. Liu, M. Wang, Y. Xu, X. Wang, X. Li, J. Liu, X. Cui, L. Jiang, Porous CoP/Co_2P heterostructure for efficient hydrogen evolution and application in magnesium/seawater battery, J. Power Sources 486 (2021), 229351.
[33] Y.-Y. Chen, Y. Zhang, X. Zhang, T. Tang, H. Luo, S. Niu, Z.-H. Dai, L.-J. Wan, J.-S. Hu, Self-templated fabrication of $MoNi_4/MoO_{3-x}$ nanorod arrays with dual active components for highly efficient hydrogen evolution, Adv. Mater. 29 (2017), 1703311.
[34] X. Lu, M. Cai, Z. Zou, J. Huang, C. Xu, A novel $MoNi@Ni(OH)_2$ heterostructure with Pt-like and stable electrocatalytic activity for the hydrogen evolution reaction, Chem. Commun. 56 (2020) 1729–1732.
[35] W. Du, Y.M. Shi, W. Zhou, Y.F. Yu, B. Zhang, Unveiling the in situ dissolution and polymerization of mo in Ni_4Mo alloy for promoting the hydrogen evolution reaction, Angew. Chem. Int. Ed. 60 (2021) 7051–7055.
[36] L. Yang, L. Zeng, H. Liu, Y. Deng, Z. Zhou, J. Yu, H. Liu, W. Zhou, Hierarchical microsphere of MoNi porous nanosheets as electrocatalyst and cocatalyst for hydrogen evolution reaction, Appl. Catal. B Environ. 249 (2019) 98–105.
[37] G. Liu, Z. Li, J. Shi, K. Sun, Y. Ji, Z. Wang, Y. Qiu, Y. Liu, Z. Wang, P. Hu, Black reduced porous SnO_2 nanosheets for CO_2 electroreduction with high formate selectivity and low overpotential, Appl. Catal. B Environ. 260 (2020), 118134.
[38] Z. Sun, Y. Wang, L. Zhang, H. Wu, Y. Jin, Y. Li, Y. Shi, T. Zhu, H. Mao, J. Liu, C. Xiao, S. Ding, Simultaneously realizing rapid electron transfer and mass transport in Jellyfish-like Mott-Schottky nanoreactors for oxygen reduction reaction, Adv. Funct. Mater. 30 (2020), 1910482.
[39] Z. Zhuang, Y. Li, Z. Li, F. Lv, Z. Lang, K. Zhao, L. Zhou, L. Moskaleva, S. Guo, L. Mai, $MoB/g\text{-}C_3N_4$ interface materials as a Schottky catalyst to boost hydrogen evolution, Angew. Chem. Int. Ed. 57 (2018) 496–500.
[40] Q. Zhang, B. Liu, L. Li, Y. Ji, C. Wang, L. Zhang, Z. Su, Maximized Schottky effect: The utrafine V_2O_3/Ni heterojunctions repeatedly arranging on monolayer nanosheets for efficient and stable water-to-hydrogen conversion, Small 17 (2021), 2005769.
[41] Y.-Y. Ma, C.-X. Wu, X.-J. Feng, H.-Q. Tan, L.-K. Yan, Y. Liu, Z.-H. Kang, E.-B. Wang, Y.-G. Li, Highly efficient hydrogen evolution from seawater by a low-cost and stable CoMoP@C electrocatalyst superior to Pt/C, Energy Environ. Sci. 10 (2017) 788–798.
[42] T. Liu, H. Liu, X. Wu, Y. Niu, B. Feng, W. Li, W. Hu, C.M. Li, Molybdenum carbide/phosphide hybrid nanoparticles embedded P, N co-doped carbon nanofibers for highly efficient hydrogen production in acidic, alkaline solution and seawater, Electrochim. Acta 281 (2018) 710–716.
[43] Q. Liu, Z. Yan, E. Wang, S. Wang, G. Sun, A high-specific-energy magnesium/water battery for full-depth ocean application, Int. J. Hydrog. Energ. 42 (2017) 23045–23053.
[44] Z. Le, W. Zhang, W. Li, J. Tan, R. Li, X. Wang, Y.V. Kaneti, X. Jiang, J. Chu, Y. Yamauchi, M. Hu, Metal-organic powder thermochemical solid-vapor architectonics toward gradient hybrid monolith with combined structure-function features, Matter 3 (2020) 879–891.
[45] Q. Qian, J. Zhang, J. Li, Y. Li, X. Jin, Y. Zhu, Y. Liu, Z. Li, A. El-Harairy, C. Xiao, G. Zhang, Y. Xie, Artificial heterointerfaces achieve delicate reaction kinetics towards hydrogen evolution and hydrazine oxidation catalysis, Angew. Chem. Int. Ed. 60 (2021) 5984–5993.
[46] S. Ramakrishnan, D.B. Velusamy, S. Sengodan, G. Nagaraju, D.H. Kim, A.R. Kim, D. J. Yoo, Rational design of multifunctional electrocatalyst: An approach towards efficient overall water splitting and rechargeable flexible solid-state zinc–air battery, Appl. Catal. B Environ. 300 (2022), 120752.
[47] S. Li, J. Jiang, N. Zhai, J. Liu, K. Feng, Y. Chen, Z. Wen, X. Sun, J. Zhong, A half-wave rectifying triboelectric nanogenerator for self-powered water splitting towards hydrogen production, Nano Energy 93 (2021), 106870.

Yingshuang Xu received his B.E. degree from Qingdao University of Science and Technology in 2019. He is currently pursuing his master's degree at Qingdao University of Science and Technology under the supervision of Prof. Luhua Jiang. His current research interests focus on new energy materials and advanced batteries, mainly including electrocatalysts for the hydrogen evolution reaction and Mg/seawater batteries.

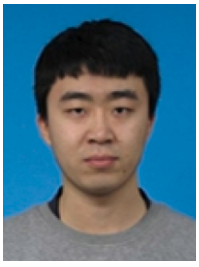

Honghao Lv received his B.E. degree from Jining University in 2020. He is currently pursuing his master's degree at Qingdao University of Science and Technology under the supervision of Prof. Luhua Jiang and associate Prof. Guangbo Liu. His current research focuses on electrocatalytic water splitting and Mg/seawater batteries.

Huasen Lu received his B.E. degree from China University of Mining and Technology in 2019. He is currently pursuing his master's degree at Qingdao University of Science and Technology under the supervision of Prof. Luhua Jiang. His current research focuses on photoelectrochemical water splitting.

Qinghao Quan received his B.E. degree from Luoyang Institute of Science and Technology in 2021. He is currently pursuing his master's degree at Qingdao University of Science and Technology under the supervision of Prof. Luhua Jiang and associate Prof. Guangbo Liu. His current research focuses on electrocatalytic water splitting.

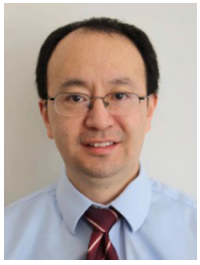

Wenzhen Li received his Ph.D. in Physical Chemistry from Dalian Institute of Chemical Physics at Chinese Academy of Sciences in 2004. He now is a professor at Iowa State University and an associate scientist for DOE Ames Lab. His main research interests include elucidating the mechanisms for electroreduction of biorenewables, carbon dioxide, nitrate, electrooxidation of alcohols and hydrogen, and electrosynthesis of hydrogen peroxide; and developing advanced electrocatalysts and electrochemical processes based on acquired new understandings.

Xuejing Cui received his master degree from Northeast University, China. He is currently a laboratory technician of College of Materials Science and Engineering, Qingdao University of Science and Technology. His main research interests focus on electrocatalysis and photoelectrocatalysis.

Guangbo Liu received his Ph.D. in Chemical Engineering and Technology from Harbin Institute of Technology in 2019. He is now an associate professor of College of Materials Science and Engineering at Qingdao University of Science and Technology. His current research focuses on design and synthesis of high-performance nanocatalysts for electrochemical water splitting and seawater batteries.

Luhua Jiang received her Ph.D. from Dalian Institute of Chemical Physics, Chinese Academy of Sciences in 2005. She is now a professor and a distinguished professor of Taishan Scholar of Qingdao University of Science and Technology, China. Dr. Jiang focuses her interests on electrocatalysis and photoelectrocatalysis related with fuel cells, seawater batteries, water splitting and carbon dioxide reduction. She has published over 150 research papers and over 80 patents. Details can be found at: https://jiang.qust.edu.cn.